International Journal of Heat and Fluid Flow 109 (2024) 109524

Contents lists available at ScienceDirect

International Journal of Heat and Fluid Flow

journal homepage: www.elsevier.com/locate/ijhff

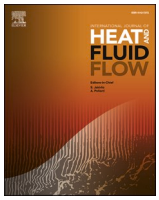

A generalised multiphase modelling approach with heat transfer and thermal phase change

H. Aburema [a,*], B.C. Hanson [a], M. Fairweather [a], M. Colombo [b]

[a] School of Chemical and Process Engineering, University of Leeds, Leeds LS2 9JT, United Kingdom
[b] Department of Mechanical Engineering, University of Sheffield, Sheffield S1 3JD, United Kingdom

ARTICLE INFO

Keywords:
Multifluid modelling approach
Interface-resolving capability
Thermal phase change
Heat transfer

ABSTRACT

The generalised multifluid modelling approach (GEMMA) was developed and implemented in OpenFOAM to address different interfacial scales in multiphase flows. The interface between two phases is tracked by adding an interface-resolving capability in computational cells occupied by large interfaces, while the model reverts to a standard multifluid formulation in regions of small/dispersed interfaces. In this work, the GEMMA model is further developed by adding the ability to predict heat transfer and thermal phase change processes. Additionally, the distinction between different interfacial scales is achieved by identifying appropriate heat transfer closures for each flow regime. The model is assessed against different test cases: predicting the condensation of single steam bubbles in subcooled water, condensation heat transfer at the interface in a steam-water co-current horizontal stratified flow, and direct contact condensation (DCC)-induced water hammer in a horizontal pipe. Comparison of simulation results with experimental data demonstrates the model successfully predicts the behaviour of condensing bubbles, heat transfer in turbulent stratified flow and effectively switches between large-interface and dispersed-interface flow regimes during the transition from a stratified into a slug flow in DCC-induced water hammer, which quantitatively captured the temperature drop due to the water hammering. Overall, the extended GEMMA model provides a comprehensive predictive tool for heat transfer and thermal phase change in multiphase flows, capable of simulating complex multiscale flows of industrial interest.

1. Introduction

Thermal phase change mechanisms, including condensation and boiling, are highly effective in transferring heat due to their capacity for substantial heat transfer rates through latent heat utilisation. Direct contact condensation (DCC), a fundamental process involving the change of state from gas to liquid driven by cooling, plays a crucial role in various industrial applications. One notable application of DCC is in nuclear reactors, particularly on free surfaces, such as those encountered in accident scenarios such as pressurised thermal shock (PTS). In PTS, injected cold water mixes with the steam present in the cold leg and other primary loop components of pressurised water reactors, contributing significantly to reactor safety by enhancing heat removal and cooling. The DCC process not only increases the cold-water temperature but can also lead to the entrapment of steam bubbles by cold water slugs. The rapid condensation of these bubbles can result in a water hammer, known as condensation-induced water hammer. Therefore, understanding the condensation process in the complex multiphase flow regimes that develop in accidents is paramount for ensuring reactor stability and mitigating hazards.

To enhance understanding of the complicated physics of DCC in stratified and slug flows, comprehensive studies have been made. Lim et al. (1984) and Kim et al. (1985) performed their experiments in a pipe, while Höhne et al. (2017) performed experiments in a horizontal channel and developed models to study direct contact condensation. In a comprehensive experimental study, Lorencez et al. (1997) measured turbulence near the free surface and analysed its influence on the interfacial heat and mass transfer coefficients. The study of Yadigaroglu (2005) highlighted the importance of comprehending the position and geometry of interfaces in specific two-phase flow situations. Particularly in scenarios where the two phases are distinctly separated, like the injection of subcooled water into a stratified pipe flow, where a detailed knowledge of the steam-water interface is crucial for precisely estimating the rate of condensation occurring within the system. DCC is particularly significant in scenarios of condensation-induced water hammer, where it acts as the driving force behind pressure surge phenomena. 35 water hammer experiments have been reported by Prasser

* Corresponding author.
E-mail address: pmhaa@leeds.ac.uk (H. Aburema).

https://doi.org/10.1016/j.ijheatfluidflow.2024.109524
Received 13 April 2024; Received in revised form 11 June 2024; Accepted 25 July 2024
Available online 7 August 2024

Nomenclature

AIAD	Algebraic Interfacial Area Density
CFD	computational fluid dynamics
DCC	direct contact condensation
EMP	Eulerian Multiphase
GEMMA	generalised multifluid modelling approach
HD	Hughes-Duffey
LES	large eddy simulation
LSI	Large-Scale Interface
IRQ	interface resolution quality
VoF	volume of fluid
A	area (m^2)
C_α	scalar field
C_p	specific heat capacity (J/kg.K)
d	diameter (m)
$D_{i,eff}$	effective thermal diffusivity (m^2/s)
F_d	drag force (N/m^3)
F_l	lift force (N/m^3)
F_{mt}	mass transfer momentum source (N/m^3)
F_{st}	surface tension force (N/m^3)
F_{td}	turbulent dispersion force (N/m^3)
F_{vm}	virtual mass force (N/m^3)
g	gravitational acceleration (m/s^2)
H	specific enthalpy (J/kg)
h	heat transfer coefficient ($W/m^2.K$)
K	kinetic energy (m^2/s^2)
k	turbulence kinetic energy (m^2/s^2)
L	latent heat (J/kg)
L_t	turbulent length scale (m)
M_i	interfacial momentum forces (N/m^3)
$\dot{m}$	mass flow rate (kg/s)
Nu	Nusselt number
P	pressure (Pa)
Pr	Prandtl number
q	heat flux (W/m^2)
Re	Reynolds number
T	temperature (K)
t	time (s)
U	velocity (m/s)
U_r	relative velocity (m/s)
U_c	compression velocity (m/s)
V	Volume (m^3)

Subscripts

b	bubble
c	continues
crit	critical
I	interfacial
LI	large interface
i	phase 1
j	phase 2
ij	phase-1dispersed in phase-2
ji	phase-2 dispersed in phase-1
max	maximum
min	minimum
sgs	Sub-grid scale
t	turbulent

Symbols

α	volume fraction
ρ	density (kg/m^3)
f	blending function
Γ	mass transfer rate ($kg/m^3.s$)
μ	dynamic viscosity (kg/m.s)
ν	kinematic viscosity (m^2/s)
δ	interface width (m)
λ	thermal conductivity(W/m.K)
τ	shear stress (N/m^2)
k	interface curvature
φ	mass flux ($kg/m^2.s$)

et al. (2004a, b), performed at the integrated thermal–hydraulic experimental facility PMK-2, located at the KFKI Atomic Energy Research Institute in Budapest, Hungary. This facility models parts of a WWER-440 nuclear power plant for safety studies, with key observations and measurements including temperature, vapour volume, local voids and water hammer pressure peak.

In addition, another important condensation process in nuclear reactors is steam bubble condensation. This process profoundly influences heat and mass transfer across the bubble interface, particularly during subcooled boiling, thereby impacting overall heat transfer efficiency and system performance. Several studies (for instance the works of Chen and Mayinger (1992), Yuan et al. (2009), Chen et al. (2010) and others) have specifically focused on experimental analysis of thermal phase change phenomena, providing valuable insights into various aspects of bubble condensation dynamics. Kim and Park (2011) investigated the condensation process of single bubbles generated from subcooled flow boiling on a wall, providing valuable insights into various aspects of bubble condensation dynamics at low pressure. The experimental study of Kamei and Hirata (1990a, b) considered single bubble condensation in subcooled water, utilising high-speed cameras to capture bubble condensation behaviours after ejection into the subcooled pool.

Despite extensive experimental efforts to understand condensation in depth, obtaining comprehensive information about this phenomenon remains challenging due to difficulties in measuring the shape and area of the interface. As a result, numerical simulations are essential as complementary tools to experimental studies. Various computational methods have been employed to track or capture the interface in two-phase systems, with volume of fluid (VoF) and coupled level set models employed successfully to simulate direct contact condensation (Pan et al., 2012; Zeng et al., 2015). Štrubelj et al. (2010) used the NEPTUNE_CFD computer code and the two-fluid model to simulate some of the cases conducted by Prasser et al. (2004b) at the PMK-2 facility. They demonstrated that the slow flooding of the pipe was abruptly interrupted by a strong slugging, followed by pressure surges induced by the water hammer. However, it is important to note that the VoF method has limitations when simulating two-phase flows with high velocity differences between the phases, as highlighted by Bartosiewicz et al. (2010) in their simulation of slug formation in an air–water channel. Moreover, such computational methods that capture all interface scales require substantial computational resources, particularly when conducting simulations in large domains or when dealing with small-scale interfaces.

Averaged Eulerian-Eulerian multifluid approaches, where interface transfer processes are modelled, are particularly effective in dispersed flow regimes, as addressed in the study of Colombo et al. (2021). This type of model, where the phases are treated as interpenetrating continua and there is no explicit tracking of the interface, has been successfully used to simulate low-Reynolds number, direct contact condensation in a suppression pool test facility (Patel et al., 2014). However, it has limitations in accurately representing large interfaces. Therefore, there is a clear need for a comprehensive multiphase modelling approach capable of handling a wide range of interfacial scales within a single

computational domain.

Recent advances in multiscale, multiphase modelling, such as the Algebraic Interfacial Area Density (AIAD) model proposed by Höhne and Vallée (2009), based on earlier work by Egorov et al. (2004), have introduced methods that bridge the gap between dispersed and large interface flows. The AIAD model distinguishes between bubbles, droplets, and the free surface using liquid volume fraction values within the computational domain, where no explicit interface detection procedure is employed, and smoothes transitions between these morphologies via a blending function. It was integrated into the CFX code and used for identifying interfacial structures in various two-phase flow scenarios, including counter-current and stratified gas–liquid flows (Höhne and Deendarlianto, 2011; Höhne et al., 2017; Höhne and Mehlhoop, 2014). In similar work, Gada et al. (2017) enhanced the Eulerian Multiphase (EMP) model in STAR-CCM+ to simulate direct contact condensation using the Large-Scale Interface (LSI) model. The LSI model distinguishes between small and large-scale interfaces based on local phase distribution, specifying closures for each regime. The LSI model allows for the modelling of surface tension effects near large-scale interfaces and treats them as moving walls using a turbulence damping procedure.

A recent development known as the generalised multifluid modelling approach (GEMMA) was developed for simulating multiscale, multiphase flows by De Santis et al. (2021). This model adjusts its formulation based on the local resolution of interfacial scales with the ability to predict multiscale, multiphase flows. When the interfacial scales are small compared to the computational mesh size, the GEMMA approach simplifies to a standard multifluid formulation, which is suitable for small or dispersed interfaces in the numerical cells. However, in cells with a fine enough mesh size to ensure a good resolution of the interfacial shape, a new multifluid formulation is introduced. This formulation is designed for simulating large or segregated interfaces and aims to mimic the behaviour of an interface-resolving approach like VoF within the multifluid framework. The GEMMA model has been rigorously evaluated against several fundamental test cases for adiabatic systems in De Santis et al. (2021) and Colombo et al. (2022). The results demonstrated its comparable accuracy to the VoF approach for cases with large or segregated interfaces, while also exhibiting standard multifluid behaviour in dispersed flows.

In this study the GEMMA model is extended to incorporate heat transfer with thermal phase change and the ability to resolve interfacial heat transfer. A critical aspect of this lies in how the model handles heat transfer and phase change processes at free surfaces and large interfaces, which profoundly impacts predictions of inter-phase heat and mass transfer. Hughes and Duffey (1991) introduced a surface renewal theory for turbulent separated flow in direct contact condensation, emphasizing turbulence's role in the liquid layer. They developed a "local" closure law to describe inter-phase heat and mass exchange in separated turbulent flows. Strubelj and Tiselj (2008) and Štrubelj et al. (2010) further advanced this approach through numerical simulations employing the NEPTUNE CFD code. In 2010, they implemented the Hughes and Duffey (1991) correlation with a two-fluid model to study DCC. Earlier, in 2008, they compared this correlation with a large interface model introduced by Coste et al. (2008), which included anisotropic friction and turbulence modelling around large interfaces. They found that the large interface model generally provided better results. Table 1 provides a summary of the main features of the models discussed above, highlighting the interface heat transfer models used and the methods for calculating the heat transfer coefficient at the interface. In the present work the approach of Hughes and Duffey (1991) is adopted since comparisons with experimental data show that their theory successfully predicts both the magnitude and the functional dependencies of condensation processes with excellent accuracy.

To assess the heat transfer and phase change model implemented in GEMMA, the model is applied to the analysis of steam bubble condensation in subcooled flows and predicting the water temperature rise in a steam-water co-current stratified flow in a horizontal channel.

Table 1
Summary of heat transfer closures used at the interface in the literature.

Publication	Model	Interphase heat transfer model	Interface heat transfer coefficient
Strubelj and Tiselj (2008)	LSI	Coste et al. (2008) $Nu = 2.7(Re)_t^{\frac{7}{8}}(\mathrm{Pr})^{\frac{1}{2}}$	$h = \frac{\lambda_c Nu}{L_t}$
Štrubelj et al. (2010)	HD	Hughes and Duffey (1991) $Nu = \frac{2}{\sqrt{\pi}}(Re)_t(\mathrm{Pr})^{\frac{1}{2}}$	
Gada et al. (2017)	LSI	Hughes and Duffey (1991) $Nu = \frac{2}{\sqrt{\pi}}(Re)_t(\mathrm{Pr})^{\frac{1}{2}}$	$h = \frac{\lambda_c A_I Nu}{\sqrt[3]{0.5\Delta V}}$
Höhne et al. (2017)	AIAD HD	Hughes and Duffey (1991) $Nu = \frac{2}{\sqrt{\pi}}(Re)_t(\mathrm{Pr})^{\frac{1}{2}}$	$h = \frac{\lambda_c Nu}{d_b}$
	AIAD Coste DCC	Coste et al. (2008) $Nu = 2.7(Re)_t^{\frac{7}{8}}(\mathrm{Pr})^{\frac{1}{2}}$	

Furthermore, the model is demonstrated to be able to switch between different flow regimes to capture the complexity of condensation-induced water hammer phenomena. In regions with large interfaces, suitable modelling closures for heat transfer are activated, while heat transfer modelling closures for dispersed flow are used in regions with small or dispersed interfaces. The accuracy of the model is assessed against different benchmark cases focusing on the key parameters of condensation and heat transfer processes through coupling with large eddy simulation employing the dynamic Smagorinsky model for the subgrid scale stress tensor. This comprehensive approach provides an accurate predictive tool for complex multiscale, multiphase flows.

2. Extended GEMMA model

The GEMMA model is developed based on the *reactingMultiphaseEulerFoam* solver, which is a part of the OpenFOAM 7.0 CFD package (Greenshields, 2019). The *reactingMultiphaseEulerFoam* solver is designed to handle a system of n compressible phases and solves conservation equations for mass, momentum and energy for each phase. The GEMMA model builds upon this framework by incorporating two different formulations within the multifluid approach. The key concept of GEMMA is the selection of one of two approaches in each computational cell based on the ability of the local grid resolution to capture the interface morphology. The Eulerian-Eulerian approach is employed in dispersed regions of the flow, where resolution of the interface on the grid is not necessary and the averaged standard multifluid representation is sufficient. On the other hand, a novel multifluid approach is utilised in regions with large interfaces, mimicking the behaviour of an interface-resolving method such as the VoF approach. The interaction between the approaches is handled using the binary C_α scalar field, which is obtained from the switch logic illustrated in Fig. 1. The main idea behind the logic is to link the activation of the large-interface mode to the local resolution of the interface morphology based on the interface resolution quality (IRQ), and the dispersed phase average diameter if a population balance is used. Minimum and maximum thresholds on the value of the volume fraction are also included to ensure that interface-resolution is only activated in the proximity of the interface. A comprehensive description of the GEMMA model can be found in De Santis et al. (2021). In this study, IRQ_{crit} is set to 2, while threshold values of 0.01 for α_{min} and 0.99 for α_{max} are used. The GEMMA model

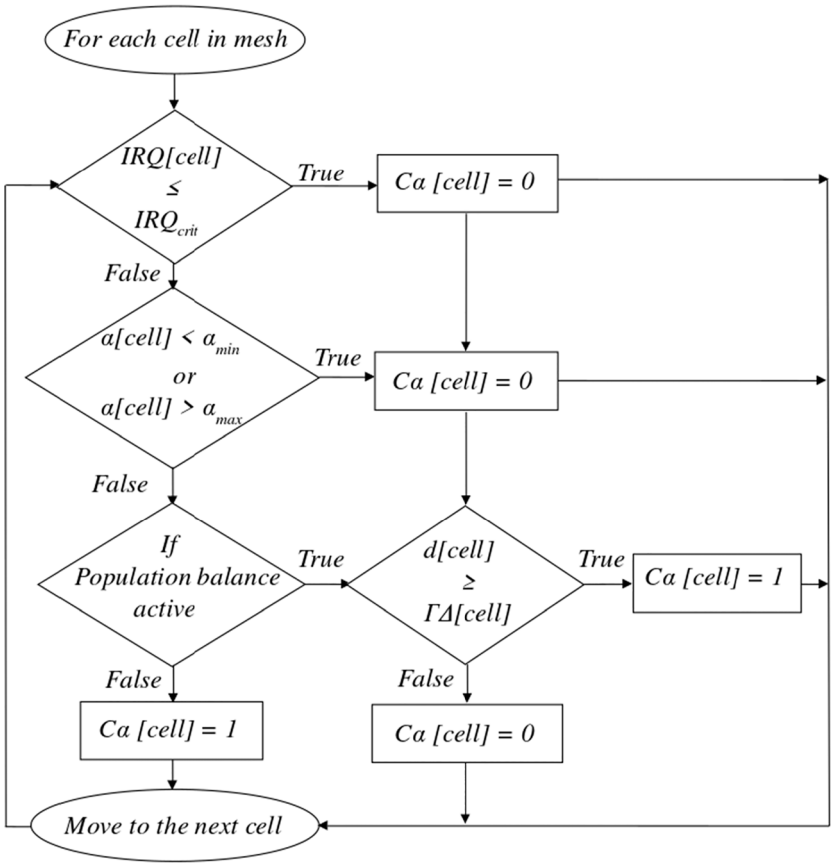

Fig. 1. Flowchart for the switching logic within GEMMA.

was originally developed to analyse adiabatic flows. However, in this study, the model has been extended to handle non-adiabatic systems by solving mass, momentum and energy conservation equations:

$$\frac{\partial(\alpha_i\rho_i)}{\partial t}+\nabla\cdot(\alpha_i\rho_i U_i)+\nabla\cdot[\alpha_i(1-\alpha_i)\rho_i U_c\,]=\Gamma_{ji}-\Gamma_{ij} \tag{1}$$

$$\frac{\partial(\alpha_i\rho_i U_i)}{\partial t}+\nabla\cdot(\alpha_i\rho_i U_i U_i)=-\alpha_i\nabla p\cdot+\alpha_i\rho_i g-\nabla\cdot(\alpha_i\tau_i)+M_i \tag{2}$$

$$\frac{\partial\left(\alpha_i\rho_i(H+K)_i\right)}{\partial t}+\nabla\cdot\left(\alpha_i\rho_i U_i(H+K)_i\right) \tag{3}$$

In Eq. (1), the compression velocity U_c is introduced to counteract numerical diffusion that affects multifluid models in the presence of sharp gradients. It is only activated at large interfaces by the C_α scalar field. The direction of the compression velocity is perpendicular to the interface and is proportional to the relative velocity between the phases, denoted as U_r:

$$U_c=C_\alpha|U_r|\frac{\nabla\alpha}{|\nabla\alpha|} \tag{4}$$

In Eq. (3), $D_{i,eff}$ indicates the phase effective thermal diffusivity, which is the sum of the laminar and turbulent diffusivities, and the last term Q_i is the energy transfer due to sensible heat transfer and phase change across the interface, and its calculation is detailed in the section 2.3. These terms are modelled using:

$$D_{i,eff}=\frac{\nu_t}{Pr_t}+\frac{\nu}{Pr} \tag{5}$$

$$Q_i=\left(\Gamma_{ji}-\Gamma_{ij}\right)H_i+h_iA_I(T_I-T_i) \tag{6}$$

2.1. Blending of interfacial transfer terms

The interfacial momentum transfer term, M_i in Eq. (2), models the dynamic interaction between the phases. This term primarily includes contributions from drag, lift, wall lubrication, turbulent dispersion, virtual mass and surface tension forces. However, when considering thermal phase change, momentum exchanges associated with the phase change mass transfer have also to be taken into account, with Γ_{ji} the mass transfer from phase j to phase i and Γ_{ij} the mass transfer from phase i to phase j (calculation of these terms is detailed in section 2.3):

$$M_i=F_d+F_l+F_{wl}+F_{td}+F_{vm}+F_{st}+F_{mt} \tag{7}$$

$$F_{mt}=\Gamma_{ji}U_j-\Gamma_{ij}U_i \tag{8}$$

In the GEMMA model, all forces are active in dispersed regimes, except for surface tension. Drag, using a specific large interface model, and surface tension are instead active when a large interface is detected. The transition between the dispersed and large interface regimes is achieved using blending models, which superimpose the switching function C_α on the standard blending methods available in OpenFOAM. For the drag force, which is active in all regimes, the blending function is given by:

$$F_d=\left(1-(1-C_\alpha)f_i-(1-C_\alpha)f_j\right)F_{d,LI}+(1-C_\alpha)f_iF_{d,ij}+(1-C_\alpha)f_jF_{d,ji} \tag{9}$$

In contrast, for forces that are considered in dispersed regimes only (i.e. lift, wall lubrication, virtual mass and turbulent dispersion), the blending is given by:

$$F_{(l,w,vm,td)}=(1-C_\alpha)f_iF_{dis,ij}+(1-C_\alpha)f_jF_{disp,ji} \tag{10}$$

2.2. Interfacial momentum transfer terms

In this study, only the drag force, phase change momentum transfer and the surface tension force play a role in the flows modelled. By using Eq. (9), the drag models can maintain the capability to cover the entire range of regimes, with the large interface drag formulation only activated in regions where such interfaces are present. In dispersed regimes, drag is modelled with the Ishii and Zuber (1979) correlation when gas is dispersed in a liquid flow, and with the Schiller and Naumann (1933) correlation when liquid is dispersed in the gas phase. Instead, for large interfaces, the drag model from Marschall (2011) is used.

$$F_{d,LI} = \left[0.5 \frac{\rho_m \delta |U_i - U_j|}{\frac{\alpha_i \alpha_j \mu_i \mu_j}{\mu_i + \mu_j}} + 8 \frac{\frac{\alpha_i \alpha_j \mu_i \mu_j}{\alpha_j \mu_i + \alpha_i \mu_j}}{\frac{\mu_i \mu_j}{\mu_i + \mu_j}} \right] \frac{|\nabla \alpha|}{\delta} \frac{\mu_i \mu_j}{\mu_i + \mu_j} (U_i - U_j) \tag{11}$$

The surface tension is considered only for large interfaces by multiplying the modelled surface tension force by C_α. In systems with significant density differences between phases, it is recommended to incorporate a density correction to model the surface tension force accurately. This correction ensures that the surface tension force depends only on the density gradient rather than the density value itself (Heyns and Oxtoby, 2014):

$$F_{st} = \alpha_i \sum_{j=1}^{n_i} \left(C_{\alpha j} \sigma_{ij} \kappa \nabla \alpha \frac{2\rho}{\Delta \rho_{ij}} \right) \tag{12}$$

Here, κ is the local interface curvature, evaluated geometrically from the volume fraction field as described by Nahed and Dgheim (2019) and modelled as $k = -\nabla \left(\frac{\nabla \alpha}{|\nabla \alpha|} \right)$ The volume fraction field in the curvature calculation is smoothed using the smoothed continuum surface force method, which involves successive interpolation cycles from cell centres to cell faces based on the approach proposed by Ubbink (1997).

2.3. Phase change model

The phase change model accounts for mass transfer due to the phase change through the interface. The model is based on the heat fluxes from the interface to each phase. The sensible heat fluxes from the interface to phase i and from the interface to the phase j are defined as follows:

$$q_i = A_I h_i (T_I - T_i) \tag{13}$$

$$q_j = A_I h_j (T_I - T_j) \tag{14}$$

The interfacial mass transfer is calculated based on the overall heat balance. The total heat flux balance to phase i and phase j is determined by solving the following equations:

$$Q_i = q_i + (\Gamma_{ji} - \Gamma_{ij}) H_i \tag{15}$$

$$Q_j = q_j + (\Gamma_{ij} - \Gamma_{ji}) H_j \tag{16}$$

The interfacial area density, A_I, for large interfaces is calculated based on the volume fraction gradient across the interface $A_I = |\nabla \alpha|$. The calculation of the mass transfer across the interface between phases can be derived by considering the overall heat balance, expressed as $Q_i + Q_j = 0$, using the following expression:

$$(\Gamma_{ji} - \Gamma_{ij}) = \frac{q_i + q_j}{L} \tag{17}$$

Here, L represents the latent heat, which is the difference between the saturation enthalpy of phase j and phase i. When the right side of Eq. (17) is positive, the mass transfer is from phase j to phase i and it is allocated in Γ_{ji}, when negative it is instead from phase i to phase j and it is allocated in Γ_{ij}. However, depending on the direction of the heat transfer, only one of these allocations exist. During condensation, only transfer from steam to water exists. By applying Eqs. (13) and (14) in Eq. (17), and considering the overall heat transfer coefficient across the interface, calculated as described in subsection 2.2, the following expression is derived:

$$(\Gamma_{ji} - \Gamma_{ij}) = \frac{A_I h \left[(T_I - T_i) + (T_I - T_j) \right]}{L} \tag{18}$$

In specific cases involving rapid condensation phenomena, the interfacial temperature is considered at saturation. In scenarios where the interface persists for a long time, the temperature between the two phases is initially considered at saturation and then updated by mass transfer from Eq. (18).

2.4. Heat transfer models

The heat transfer coefficient in regions of small/dispersed interfaces is calculated from the Nusselt number Nu as:

$$h = \frac{\lambda_c Nu}{d_b} \tag{19}$$

where d_d is the dispersed phase diameter. The correlation of Hughmark (1967) has been implemented as one of the typical models used to determine the phase change coefficient based on comparisons made between different experimental correlations (Li et al., 2022), and is used in Eq. (19) as:

$$Nu = 2 + 0.27 Re^{0.5} Pr^{\frac{1}{3}} \tag{20}$$

Where the Reynolds number, Re, and the Prandtl number, Pr, are calculated as:

$$Re = \frac{U_r d_b}{\nu_c} \tag{21}$$

$$Pr = \frac{\nu_c C_p \rho_c}{\lambda_c} \tag{22}$$

In the case where a segregated/large interface is present, the interfacial heat transfer coefficient is calculated as a function of the Nusselt number and the interface width as:

$$h = \frac{\lambda_c Nu}{\delta} \tag{23}$$

Here, in Eq. (23), the model of Hughes and Duffey (1991) is adopted, which has been validated for a concurrent horizontal stratified flow of steam-water in a rectangular channel. The Nusselt number formulation is defined as:

$$Nu = 1.13 Re_t Pr^{\frac{1}{2}} \tag{24}$$

where Re_t is calculated as:

$$Re_t = \frac{U_t L_t}{\nu_c} \tag{25}$$

where L_t is a turbulent length scale, and $U_t = (2k/3)^{0.5}$ is the turbulent velocity. The generalised blending method within GEMMA has undergone further development to incorporate closures for the interfacial heat transfer term. This extension enables the use for heat transfer models of the same blending formula employed for drag models in Eq. (9). In dispersed regimes, the Ranz and Marshall (1952a, b) or Hughmark (1967) correlations can be used. Conversely, for large interfaces, the Hughes and Duffey (1991) model is applied.

2.5. Large eddy simulation

In large eddy simulation (LES), the fluid flow field is divided into resolved large-scale motions that are directly computed and small-scale sub-grid fluctuations, which are not explicitly resolved. The velocity field in Eqs. (1)–(3) represents the resolved velocity contribution, which is obtained by performing filtering (volume averaging) of the governing equations. The unresolved sub-grid scale (SGS) stress tensor must be modelled to close the equation set. The SGS stress tensor is related to the resolved scale strain tensor (S_{ij}) and the SGS turbulent viscosity (ν_{sgs}) according to:

$$\tau_{ij} = -2\nu_{sgs}\overline{S_{ij}} - \frac{1}{3}\delta_{ij}\tau_{kk} \tag{26}$$

$$\overline{S_{ij}} = \frac{1}{2}\left(\frac{\partial\overline{U_i}}{\partial x_j} + \frac{\partial\overline{U_j}}{\partial x_i}\right) \tag{27}$$

The most widely used SGS model is the Smagorinsky model, which relies on a predefined constant (Smagorinsky, 1963). The turbulent viscosity is computed by multiplying the filter width (Δ), in this work taken as the grid spacing, by the magnitude of the strain rate tensor and the model constant as follows:

$$\nu_{sgs} = (C_s\Delta)^2\left|\overline{S_{ij}}\right| \tag{30}$$

By applying a second filter, known as the test filter, a dynamic version of this model considers both spatial and temporal variations, which doubles the mesh size in the present study. This procedure is standard, and further details can be found in Germano et al. (1991), Germano (1992) and Lilly (1992). The precision of the model is improved by accounting for such variations, making it more dependable for capturing flow dynamics than the basic Smagorinsky model. For accurate results, the dynamic SGS model is used in this study. It employs a dynamic procedure to calculate C_s based on the resolved stress tensor L_{ij} and the Germano rate of strain tensor M_{ij} through an iterative process (Germano et al., 1991):

$$C_s = \frac{1}{2}\frac{L_{ij}M_{ij}}{M_{ij}M_{ij}} \tag{31}$$

where

$$L_{ij} = \overline{\overline{U_iU_j}} - \overline{\overline{U_i}\,\overline{U_j}} \tag{32}$$

$$M_{ij} = \Delta^2\overline{\overline{S_{ij}}\left|\overline{S_{ij}}\right|} - \overline{\Delta^2\overline{S_{ij}}\left|\overline{S_{ij}}\right|} \tag{33}$$

Many studies have utilized the Euler-Euler two-fluid model with LES for dispersed phase flow. In these models, researchers incorporate bubble-induced turbulence effects into LES by adding an additional term to the SGS turbulent viscosity (Ma et al., 2015; Ma et al., 2016; Long et al., 2020). However, in the specific cases considered in this study, bubble-induced turbulence does not contribute significantly as large interface (stratified flow) is the dominant regime. Accordingly, LES is applied to both phases in these cases.

3. Simulation set-up

3.1. Single bubble condensation

To the first case studied, the computational setup is designed to investigate the condensation of a bubble that detaches from a wall in a boiling flow, subsequently rises and condenses in a subcooled flow. The simulation considers both two- and three-dimensional space domains, where the dimensions are defined as 2*d*, 5*d*, and 2*d* in the *x*, *y* and *z* directions, respectively, as shown in Fig. 2a. The initial diameter of the bubble is denoted as *d*, and the spherical bubble is initialised at position (*d*, *d*, *d*). A grid size of 75 × 150 × 75 is employed for the simulation. The boundary conditions are listed in Table 2. By adopting this approach, the simulation effectively replicates the behaviour of a detached bubble in a realistic boiling and condensation scenario with low velocity fluid flow.

3.2. Co-current stratified steam-water flow

In the second test case, the computations replicate the experiment of Höhne et al. (2017), conducted to study steam-water stratified flow in a 1.2 m long horizontal channel with a cross-section of 0.1 m × 0.02 m (height × width), which included a 0.163 m long metal plate separating the two flows at the inlet. However, for the purpose of simplicity, the metal plate was not included in the computational domain and the starting point of the channel was shifted to the end of this plate in the present work.

Water enters the channel at a subcooled temperature of 293 K with a

Table 2
Boundary conditions for the bubble condensation simulations.

Boundary	Bottom	Top	Side walls
Volume fraction	Fixed value	Zero gradient	Zero gradient
Velocity	Fixed value	Zero gradient	No-slip
Pressure	Fixed pressure gradient	Total pressure	Fixed pressure gradient
Temperature	Fixed value	Zero gradient	Zero gradient

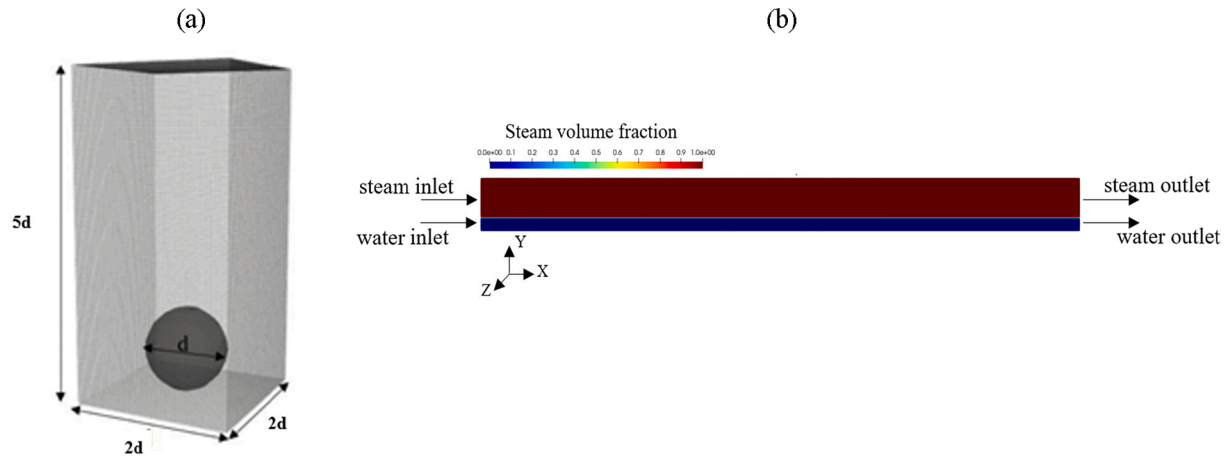

Fig. 2. (a) The three-dimensional computational domain for the rising bubble case and (b) steam volume fraction in the steam-water stratified horizontal channel flow.

flow rate of 49.7 m^3/h, while steam is injected at the saturated temperature corresponding to the pressure in the channel with walls thermally insulated. Therefore, the steam above the free surface is treated as an isothermal gas with known constant properties. The three-dimensional geometry was discretised into approximately 2.4 million hexahedral cells, and adiabatic walls were implemented with a no-slip boundary condition applied to both continuous phases at the walls. The outlet boundary condition was set as a pressure boundary. Table 3 provides the total number of mesh elements (N), the number of elements in each direction (N_x, N_y, and N_z), and the refinement in the streamwise and vertical directions (Δx and Δy), together with an overview of the simulation settings and boundary conditions. At the beginning of the simulation, the water level was set to 0.025 m (Fig. 2b). The Reynolds number of the steam was 9,000, and a turbulence intensity of 5 % was assumed at the inlet. The velocity of the steam and the water at the inlet were 6 m/s and 0.028 m/s, respectively. Initially, the volume fraction of water was set to unity in the lower part of the channel, while the volume fraction of steam was set to unity in the upper part.

3.3. Steam induced water hammer

For the condensation-induced water hammer case, we considered the experiments conducted on the steam-line of the PMK-2 device at the Hungarian Atomic Energy Research Institute KFKI (Prasser et al., 2004a, b). Fig. 3a shows a schematic of the experimental rig. The pipe geometry consists of a 3,200 mm horizontal pipe (measured from the water inlet on the left side to the steam inlet on the right side) with an inner diameter of 73 mm, together with a 1,007 mm long vertical linear pipe of the same diameter. The main part of the test section covers 2,800 mm along the horizontal section of the pipe. Steam is supplied to the test section from the top right end of the pipe via a steam generator, and water from a 75-litre tank is injected into the main pipe through a smaller 24 mm diameter pipe attached to the lower horizontal section. According to Prasser et al. (2004a, b), 35 water hammer experimental results were obtained from the PMK-2 experiments under various conditions. These results were collected using three types of sensors: a wire-mesh sensor, a temperature sensor, and three pressure transducers, with their specific locations illustrated in Fig. 3a. In the experiment selected for the simulation, the system was operated at a pressure of 35 bar, with cold water entering at a rate of 1.0 kg/s at 123 °C, as illustrated in Fig. 3b. Initial conditions reflected the pipe filled with steam at saturation temperature. The boundary conditions included the mass flow rate of water and pressure at the steam inlet (Table 4).

4. Results and discussion

This section presents predictions of the GEMMA model for the test cases discussed in Section 3. Results are analysed to evaluate the model's accuracy in capturing the condensation behaviour of a steam bubble in subcooled water, and multiphase phenomena at a stratified interface, particularly the condensation and heat transfer dynamics. By comparing simulations with experimental data, this section provides insights into the model's predictive capabilities and effectiveness in addressing multiphase flow behaviours.

Table 3
Mesh parameters and simulation settings used in stratified steam water flow.

	N	N_x	N_y	N_z	Δx [m]	Δy [m]
Mesh	2.4	600	143	20	0.002	0.001–0.0002
Turbulence (both phases)	LES with dynamic SGS model					
Water level [m]	0.025					
Steam direction	Co-current					
Boundary conditions	**Temperature**		**Velocity**		**Pressure**	
Inlet	Fixed value		Fixed value		Zero gradient	
Outlet	Zero gradient		Zero gradient		Fixed value	
Walls	Zero gradient		No-slip		Zero gradient	

4.1. Single bubble condensation

To validate the modified GEMMA model, simulations of condensing bubbles were performed and compared with published experimental results under the conditions shown in Table 5. The behaviour of an adiabatic bubble is also compared with a condensing bubble for one of the considered cases. A comparison of bubble diameter history is presented in Fig. 4, contrasting the predictions of a two-dimensional model with the experimental data of Kamei and Hirata (1990b). Although the numerical results exhibit reasonable agreement with the experimental data, there is a tendency for under-prediction attributed to the assumption of a spherical bubble shape in simulations, which differs from the irregular shapes observed in real experiments. Nonetheless, despite this disparity, the 2D simulation follows a similar trend of condensation, indicating a promising alignment between the model's predictions and the observed behaviours.

The predictions of condensation from both two- and three-dimensional simulations are compared for case 3 in Fig. 5a and Fig. 5b. In general, the bubble diameter history of both simulation types agrees well with the experimental data and reasonably predicts the bubble condensation process. Fig. 6a presents a comparison of the condensation process for case 4. Although both simulations show less agreement with the experimental data (Kim and Park, 2011) due to the initial spherical shape assumption in the simulations, unlike the irregularly shaped bubbles in the experiment, the simulated bubbles still demonstrate a similar trend of volume decrease over time as observed experimentally. In Fig. 6b, the simulation of bubble volume over time is compared with experimental data. Here, the two-dimensional simulation tends to over-predict the volume, while the three-dimensional simulation under-predicts it; however, both simulations still exhibit satisfactory agreement with the experimental data. This difference in the predictions is attributable to the fact that the three-dimensional model more accurately represents the bubble volume and hence buoyancy, as present in the experiment. Furthermore, it is worth noting that smaller bubbles tend to exhibit a nearly spherical and symmetrical shape, making the approximation in the simulation more appropriate, as observed in case 3.

Fig. 7a illustrates the time-dependent behaviour of the condensing bubble and an adiabatic bubble for case 4, allowing for a qualitative comparison. Through analysis of the results, it is evident that the deformation behaviour of the condensing bubble differs from that of the adiabatic bubble. In the adiabatic bubble case, the bubble rises in the water while maintaining its initial size. The hydrodynamic force is responsible for deforming the bubble, causing it to transition from a spherical shape to an elliptical shape and eventually to a hemispherical shape. In addition, Fig. 7b illustrates the interfacial condensation rate along the two-dimensional surface of the condensing bubble at 2 ms for case 4. The simulation results demonstrate satisfactory agreement with the experimental results of Kim and Park (2011), both in terms of time and bubble volume. It is worth noting that the condensation rates are almost symmetric on both sides of the bubble, resulting in a symmetric shape.

In Fig. 8, the evolution of the bubble's shape during the deformation process is displayed, and the predictions are compared with data from Kamei and Hirata (1990a). Initially, the bubble is observed in the experiment to become flattened due to buoyancy (1 ms), then transitions into a hemispherical shape as mass transfer comes into play (1.5 ms). Later, the top of the bubble flattens, resulting in an oval shape (2.5 ms).

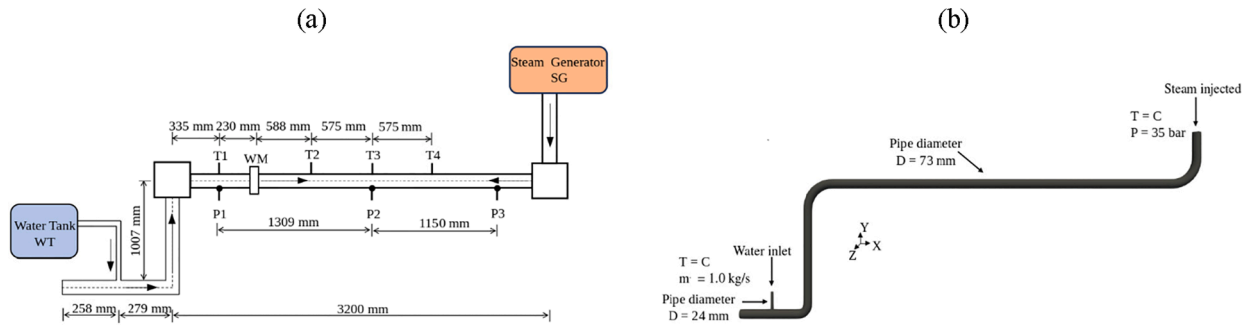

Fig. 3. (a) Schematic view of the PMK-2 KFKI experimental rig, and (b) sketch of the test section.

Table 4
Boundary conditions of the computational simulation of steam induced water hammer.

Boundary	Inlet	Outlet	Walls
Volume fraction	Fixed value	Zero gradient if flows out, and fixed value if flows into the domain	Zero gradient
Velocity	Fixed flow rate	Inlet specified from outlet	No-slip
Pressure	Zero gradient	Fixed pressure	Zero gradient
Temperature	Fixed value	Inlet specified from outlet	Zero gradient

Table 5
Operating conditions for experimental cases.

Case number	Source	P [MPa]	ΔT_{sat} [K]	φ[kg/m^2 s]	d_b [mm]
1	Kamei and Hirata, 1990b	0.106	8.7	100	1.024
2	Kamei and Hirata, 1990b	0.101	12.8	118	0.950
3	Kamei and Hirata, 1990b	0.130	25	400	1.008
4	Kim and Park, 2011	0.105	12	85	4.9
5	Kamei and Hirata, 1990a	0.2	10	–	8.0

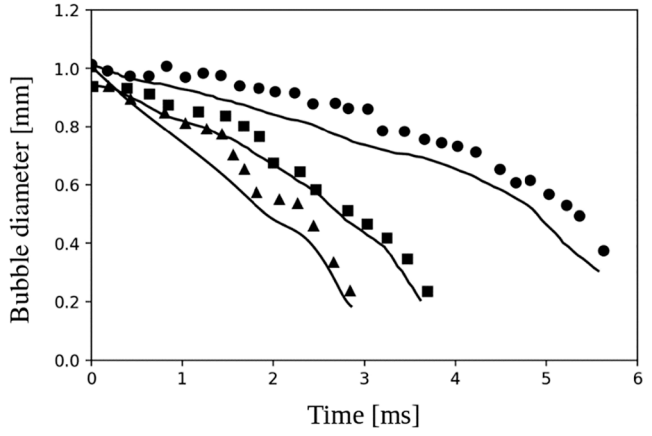

Fig. 4. Comparison of bubble diameter history between experimental cases (●) 1, (■) 2 and (▲) 3 and (▬) two-dimensional simulations.

Eventually, the bubble returns to its spherical shape (4.5 ms) due to the increased influence of surface tension. This behaviour, particularly the transition from a flat to an oval shape, can be attributed to the size of the bubble, which influences the dynamics of mass transfer and surface tension. Larger bubbles tend to exhibit different behaviour compared to smaller ones due to factors such as buoyancy, inertia and surface tension effects. Despite these variations, the historical trend of the predicted bubble shape closely aligns with the experimental observations, demonstrating good agreement between the simulation and experimental data.

4.2. Co-current stratified steam-water flow

The primary goal of this simulation is to assess the accuracy of the model in predicting the increase in water temperature caused by interfacial heat transfer and condensation at a stratified interface in a rectangular channel. Results are compared against the experiment conducted by Höhne et al. (2017). The simulation results corresponding to the experiment (Höhne et al., 2017) are presented below for analysis. Throughout the condensation process, the specific heat associated with the phase transition is released and entirely utilised to elevate the temperature of the initially subcooled water.

Fig. 9 displays the predicted temperature distribution along the horizontal channel during the condensation process. Notably, the most significant heating of the injected cold water is observed closer to the outlet of the channel rather than near the inlet. This observation can be attributed to the longer contact time between the water and the saturated steam in that specific region. The difference in velocities between the water and steam leads to prolonged interaction, facilitating more efficient heat transfer and resulting in a more pronounced temperature elevation.

Fig. 10a presents the temperature profiles on a horizontal measurement plane located just below the water surface. Notably, there is a consistent rise in water temperature along the channel, due to steam condensation and related heat transfer to the water side. The simulation results closely match the experimental data in the initial part of the channel, but they tend to over-predict the water temperature near the outlet. The temperature profiles at three horizontal distances from the inlet ($x = 0.25$ m, 0.6 m and 1.0 m) shown in Fig. 10b demonstrate a consistent upward trend in water temperature towards the outlet of the channel. The increase in vertical temperature, moving upwards from water to steam, can be attributed to the heat transfer occurring between the steam and water phases. In this flow regime, steam and water exist in separate layers due to density differences, creating a stratified flow. As the steam condenses into the water at the interface, heat is released and transferred from the steam phase to the water phase, leading to a temperature rise as one moves vertically upwards. Although the predictive accuracy decreases in the first half part of the channel, it is restored towards the end of the channel. There is a deviation at $y = 0.023$ m, as previously shown in Fig. 10a, but below that level, the agreement with data is good.

4.3. DCC-induced water hammer

In this case, the primary objective is to assess how well the model

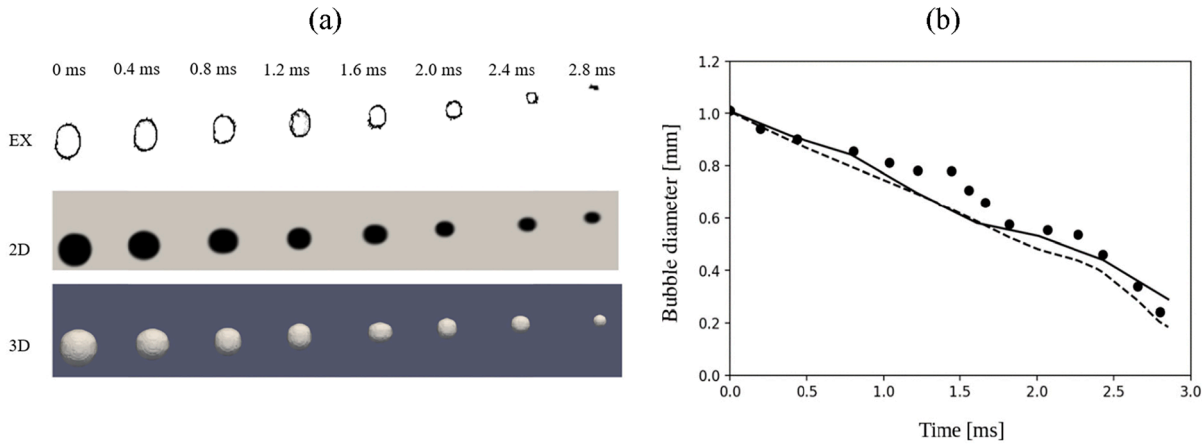

Fig. 5. (a) Bubble shape history comparison between (EX) experiment, (2D) two- and (3D) three-dimensional simulations for case 3, and (b) bubble diameter history comparison between (●) experiment, and (– – – –) two- and (▬) three-dimensional simulations for case 3.

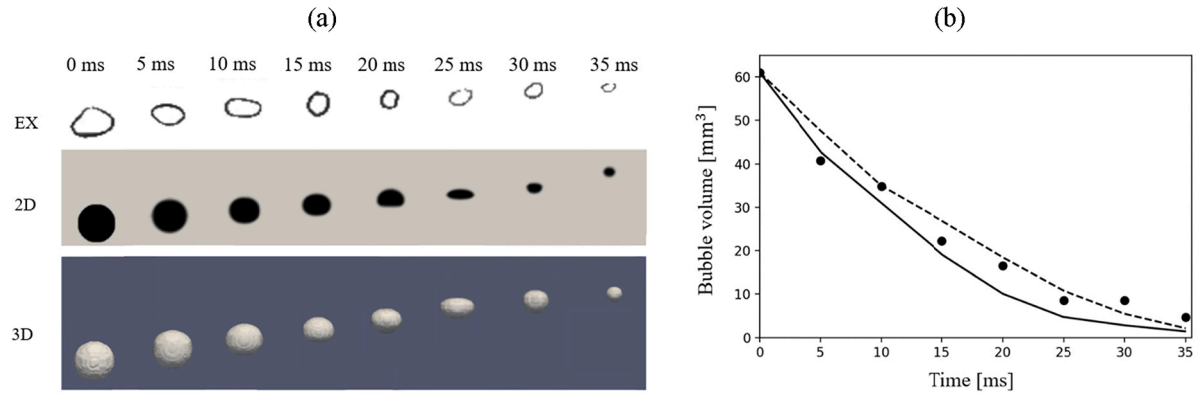

Fig. 6. (a) Bubble shape history comparison between (EX) experiment, (2D) two- and (3D) three-dimensional simulations for case 4, and (b) bubble volume history comparison between (●) experiment, and (– – – –) two- and (▬) three-dimensional simulations for case 4.

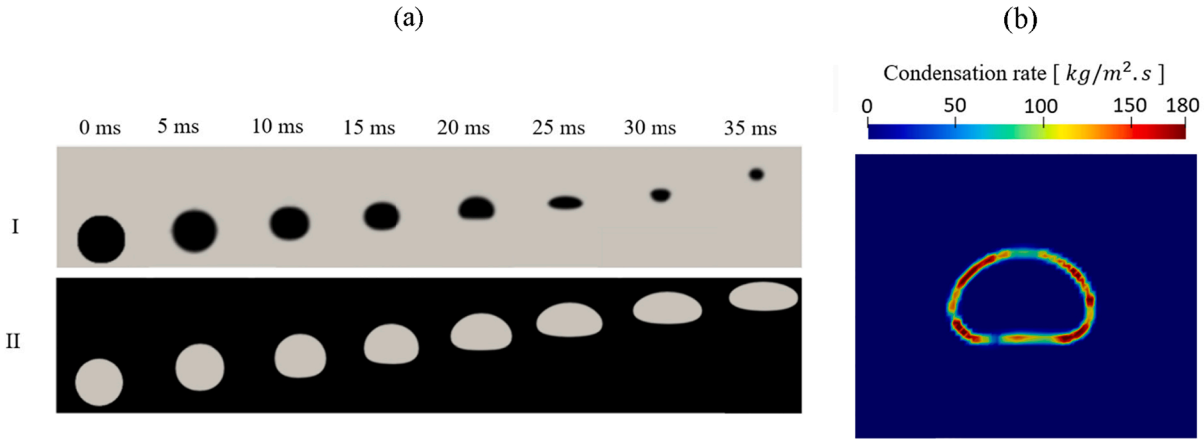

Fig. 7. (a) Two-dimensional bubble shape history comparison between (I) condensing system and (II) adiabatic bubble for case 4, and (b) interfacial condensation rate at 2 ms for case 4.

predicts the rise in water temperature during the condensation-induced water hammer experiment, which corresponds to the increase in water level resulting from flooding during these scenarios. This is achieved by examining local temperature measurements and forecasting the temporal evolution of temperature at specific locations. The comparison between the water level measurements obtained from the wire-mesh sensor during experimental trials and the predictions generated by the GEMMA model is shown in Fig. 11. It is clear that there is a noticeable difference in the timing of the water level rise, especially between $t =$ 7.5 s and 11.5 s, which is likely due to the influence of the flooding wave observed in the results below. Interestingly, this difference is less pronounced in the simulation results compared to the experimental data. Additionally, the GEMMA model accurately predicts the moment when the water level reaches the top of the pipe, aligning closely with when

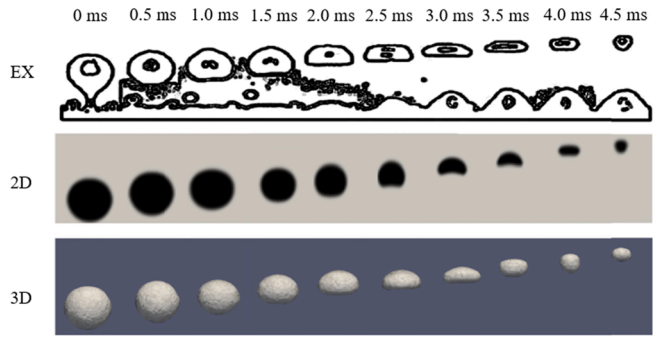

Fig. 8. Bubble shape history comparison during condensation for case 5.

water enters the horizontal pipe section.

In Fig. 12, the simulation illustrates local temperature variations, compared with measurements made during the experiment (Prasser et al., 2004a, b) at points T1–T4. At point T1, there is a drop in temperature as the water floods the area. Notably, the GEMMA model accurately predicts the onset of this flooding. A sudden decrease in temperature is observed at around $t = 13$ s, indicating the arrival of cold water at the probe location, aligned with the observed increase in water level in Fig. 11. In the simulation, the ultimate decrease in temperature of the water at measuring point T1 is slightly under-estimated. This is because the temperature continues to decrease as cold water is continuously injected into the system. Approximately 0.7 s prior to the experimental observation, the model predicts flooding at measuring point T2. Although the measured peak temperature is not predicted, temperature fluctuations during the temperature drop are, indicating the possibility of water waves caused by unstable flow. Multiple water flooding waves are observed in the experiment at measuring point T3. While the model accurately predicts the formation of a liquid slug near T3 between $t = 10$ s and 12 s, which is also observed in the experiment, at measuring point T4 the same phenomenon appears with a 2 s delay in the simulation. Although temperatures in the simulation may not precisely match experimental ones due to uncertainties regarding probe positioning and data collection, overall agreement is satisfactory. Additionally, the experimental results are for a single realisation, with ensemble-averaged data unavailable, making the accurate prediction of a complex experimental flow, where initial conditions are likely to vary, difficult.

Fig. 12 also compares the present predictions with the numerical results from the work of Štrubelj et al. (2010) which used a large interface model at the stratified interface. The Štrubelj et al. (2010) simulations effectively model the temperature drop at T1 at the appropriate time, followed by a gradual decrease in water temperature until it stabilises at a specific value. In their simulation, flooding at T2 occurs after 0.75 s of the experiment, resulting in the observation of two peaks (or slugs). However, their predictions at measuring points T3 and T4 do not accurately capture the flooding waves and the temperature drops.

The temporal progression of the interface predicted using the GEMMA model is illustrated through contour plots of water volume-fraction in Fig. 13a at $t = 7$, 10 and 12 s. At $t = 7$ s, water has flooded both the lower horizontal and vertical sections, resulting in a planar interface with no vapour entrapped. By $t = 10$ s, the reflection of the flooding wave begins from the end of the pipe due to counter-current steam flow over the interface. At $t = 12$ s, the water contacts the pipe wall near the position of the wire-mesh sensor. The temperature rise of the injected cold water is mostly observed away from the vertical inlet in the horizontal pipe section, as shown in Fig. 13b, where it remains in contact with saturated steam for a long duration. This extended contact

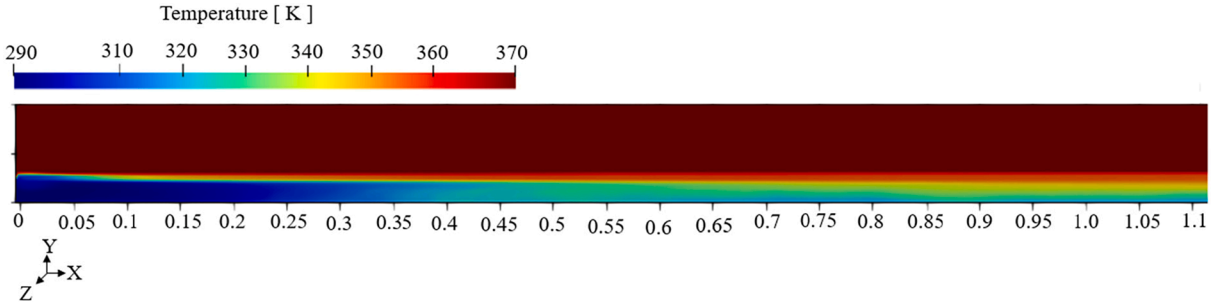

Fig. 9. Temperature distribution of the water along the central plane of the channel.

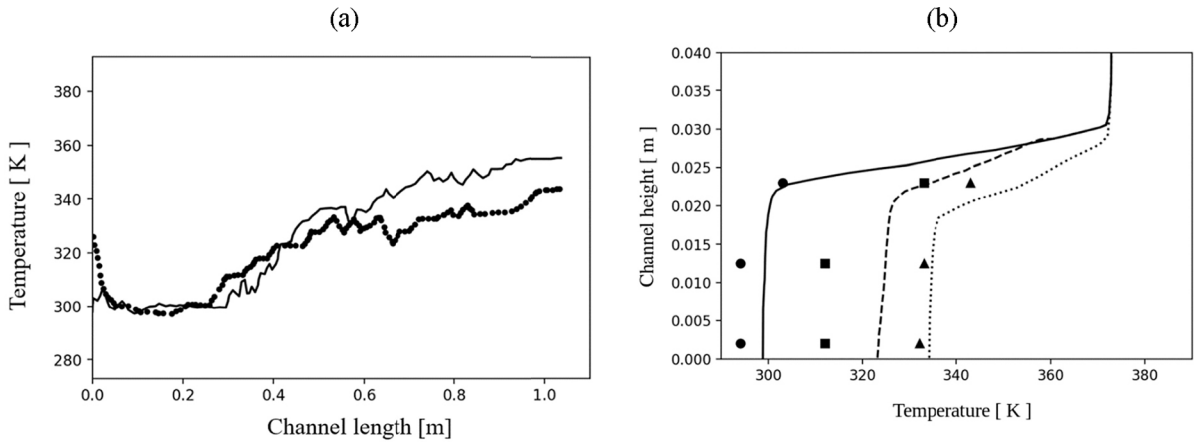

Fig. 10. Comparison of water temperature: (a) between (●) experiment and (▬) GEMMA model along the channel at a fixed height of $y = 0.023$ m, and (b) at different positions along the channel ($x = 0.25$ m; (●) experiment and (▬) GEMMA model), ($x = 0.6$ m; (■) experiment and (– – – –) GEMMA model), and ($x = 1.0$ m; (▲) experiment and (···) GEMMA model). In (b), measurements are only available at heights $y = 0.002$ m, 0.0125 m and 0.023 m).

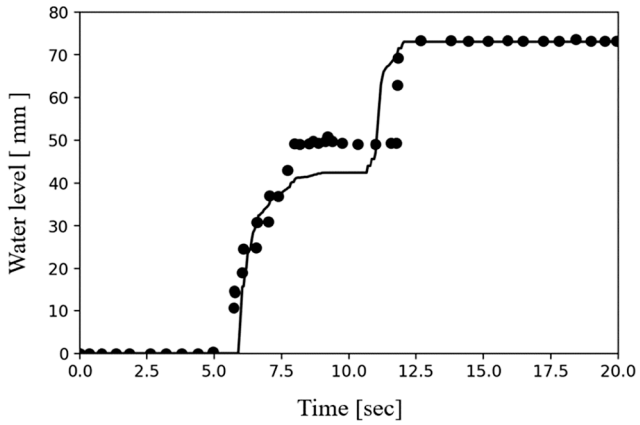

Fig. 11. Water level in horizontal pipe at 565 mm, (●) experiment and (▬) GEMMA model.

allows the cold water to absorb heat from the steam, gradually raising its temperature. Consequently, by the time the water reaches the end of the pipe section, nearly all of it has reached saturation temperature.

5. Conclusions

In this study, the extended GEMMA model, incorporating thermal phase change, was effectively used to simulate heat transfer and condensation in multiple multiphase regimes and for interfaces of significantly different scale. The model was first used to predict the condensation of single steam bubbles in a subcooled flow. The model's performance was thoroughly validated through a comprehensive investigation involving various initial bubble diameters. By comparing changes in bubble shape during the condensation process with experimental images, and the reduction in bubble volume with time, the simulations demonstrated a satisfactory level of agreement with experimental data. This ability to accurately capture the dynamics of steam bubble condensation is particularly significant in applications such as nuclear reactors, where such processes significantly impact heat and mass transfer rates. Moreover, the successful validation study showcases the GEMMA model's ability to offer reliable predictions and insights into complex interfacial heat transfer phenomena associated with direct contact condensation. Specifically, the validation process was extended to examine the GEMMA model's performance in predicting heat and mass transfer between steam and water in a turbulent stratified channel flow. The results indicated a consistent increase in water temperature towards the outlet of the channel, reflecting effective heat transfer from steam to water. Additionally, it is noteworthy to mention the inclusion of the case of condensation-induced water hammer in the study. By accurately simulating this phenomenon, the extended GEMMA model demonstrates its versatility and applicability in capturing a wide range of multiphase flow scenarios with industrial relevance. This enhanced predictive capability holds significant promise in supporting applications such as nuclear reactor safety analysis and industrial process optimisation. However, uncertainties regarding the exact positioning of local void probes with integrated thermocouples inside the experimental rig, and the precise location of data collection in the experiments, potentially led to discrepancies between the predictions and experimental measurements. Analysis uncovered an over-estimation of water temperature, highlighting the need for further improvement in the heat transfer model, particularly for large interfaces. To address this issue, future development efforts will focus on refining the heat transfer model to better represent interfacial heat and mass transfer dynamics. This targeted development aims to achieve more accurate predictions of water temperature distributions, thereby enhancing the overall

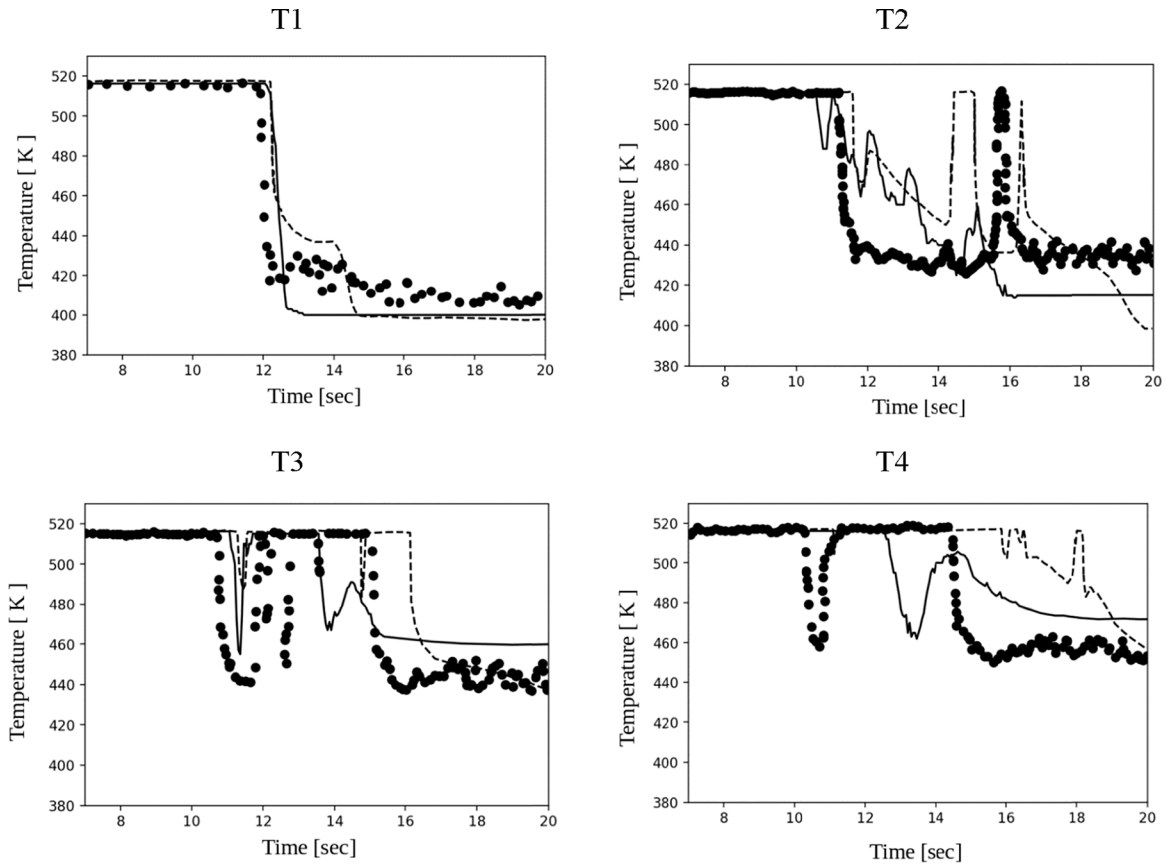

Fig. 12. Local temperature measurements at points T1, T2, T3 and T4; (●) experiment, (▬) GEMMA model and (– – – –) Štrubelj et al. (2010) predictions.

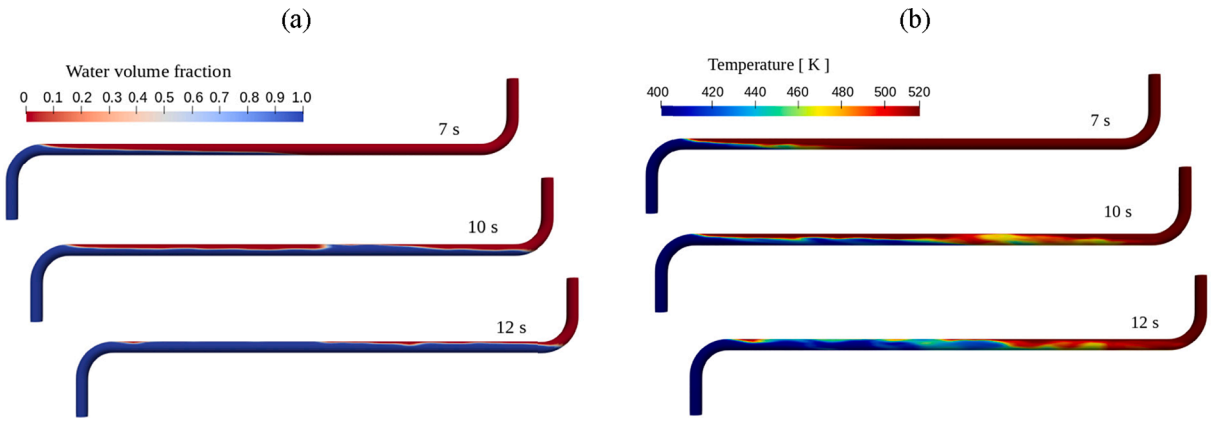

Fig. 13. (a) Water volume fraction and (b) field temperature at times 7 s, 10 s and 12 s.

reliability of multiphase flow simulations.

CRediT authorship contribution statement

H. Aburema: Writing – original draft, Methodology. **B.C. Hanson:** Writing – review & editing, Methodology. **M. Fairweather:** Writing – review & editing, Methodology. **M. Colombo:** Writing – review & editing, Methodology.

Declaration of competing interest

The authors declare the following financial interests/personal relationships which may be considered as potential competing interests: Hanan Aburema reports financial support was provided by Ministry of Higher Education and Scientific Research of Libya. If there are other authors, they declare that they have no known competing financial interests or personal relationships that could have appeared to influence the work reported in this paper.

Data availability

Data will be made available on request.

Acknowledgments

This work is supported by the Ministry of Higher Education and Scientific Research of Libya.

References

Bartosiewicz, Y., Seynhaeve, J.-M., Vallée, C., Höhne, T., Laviéville, J.-M., 2010. Modelling free surface flows relevant to a PTS scenario: Comparison between experimental data and three RANS based CFD-codes. Comments on the CFD-experiment integration and best practice guideline. Nucl. Eng. Des. 240 (9), 2375–2381. https://doi.org/10.1016/j.nucengdes.2010.04.032.

Chen, Y.M., Mayinger, F., 1992. Measurement of heat transfer at the phase interface of condensing bubbles. Int. J. Multiph. Flow 18 (6), 877–890. https://doi.org/10.1016/0301-9322(92)90065-O.

Chen, D., Pan, L., Yuan, D., Wang, X., 2010. Dual model of bubble growth in vertical rectangular narrow channel. Int. Commun. Heat Mass Transf. 37 (8), 1004–1007. https://doi.org/10.1016/j.icheatmasstransfer.2010.06.023.

Colombo, M., Rzehak, R., Fairweather, M., Liao, Y., Lucas, D., 2021. Benchmarking of computational fluid dynamic models for bubbly flows. Nucl. Eng. Des. 375, 111075 https://doi.org/10.1016/j.nucengdes.2021.111075.

Colombo, M., De Santis, A., Hanson, B.C., Fairweather, M., 2022. Prediction of horizontal gas-liquid segregated flow regimes with an all flow regime multifluid model. Processes 10 (5), 920. https://doi.org/10.3390/pr10050920.

Coste, P., Pouvreau, J., Laviéville, J., Boucker, M., 2008. A two-phase CFD approach to the PTS problem evaluated on COSI experiment. In: Proceedings of the 16th International Conference on Nuclear Engineering ICONE16, Orlando, USA, 11-15 May.

De Santis, A., Colombo, M., Hanson, B.C., Fairweather, M., 2021. A generalized multiphase modelling approach for multiscale flows. J. Comput. Phys. 436, 110321 https://doi.org/10.1016/j.jcp.2021.110321.

Egorov, Y., Boucker, M., Martin, A., Pigny, S., Scheuerer, M., Willemsen, S., 2004. Validation of CFD codes with PTS-relevant test cases. In: 5th Euratom Framework Programme, Tech. Rep. EVOL-ECORA-D07.

Gada, V.H., Tandon, M.P., Elias, J., Vikulov, R., Lo, S., 2017. A large scale interface multi-fluid model for simulating multiphase flows. Appl. Math. Model. 44, 189–204. https://doi.org/10.1016/j.apm.2017.02.030.

Germano, M., 1992. Turbulence: the filtering approach. J. Fluid Mech. 238, 325–336. https://doi.org/10.1017/S0022112092001733.

Germano, M., Piomelli, U., Moin, P., Cabot, W.H., 1991. A dynamic subgrid-scale eddy viscosity model. Phys. Fluids 3 (7), 1760–1765. https://doi.org/10.1063/1.857955.

Greenshields, C.J., 2019. OpenFOAM v7 User Guide [www document]. CFD Direct Ltd. accessed 3.8.24 https://github.com/OpenFOAM/OpenFOAM-7/blob/master/doc/Guides/OpenFOAMUserGuide-A4.pdf.

Heyns, J.A., Oxtoby, O.F., 2014. Modelling surface tension dominated multiphase flows using the VOF approach. In: Proceedings of the 6th European Conference on Computational Fluid Dynamics, Barcelona, Spain, 20-25 July.

Höhne, T., Deendarlianto, D.L., 2011. Numerical simulations of counter-current two-phase flow experiments in a PWR hot leg model using an area density model. Int. J. Heat Fluid Flow 32, 1047–1056. https://doi.org/10.1016/j.ijheatfluidflow.2011.05.007.

Höhne, T., Mehlhoop, J.P., 2014. Validation of closure models for interfacial drag and turbulence in numerical simulations of horizontal stratified gas-liquid flows. Int. J. Multiph. Flow 62, 1–16. https://doi.org/10.1016/j.ijmultiphaseflow.2014.01.012.

Höhne, T., Vallée, C., 2009. Modelling of stratified two phase flows using an interfacial area density model. WIT Trans. Eng. Sci. 63, 23–133.

Höhne, T., Gasiunas, S., Šeporaitis, M., 2017. Numerical modelling of a direct contact condensation experiment using the AIAD framework. Int. J. Heat Mass Transf. 111, 211–222. https://doi.org/10.1016/j.ijheatmasstransfer.2017.03.104.

Hughes, E.D., Duffey, R.B., 1991. Direct contact condensation and momentum transfer in turbulent separated flows. Int. J. Multiph. Flow 17 (5), 599–619. https://doi.org/10.1016/0301-9322(91)90027-Z.

Hughmark, G.A., 1967. Mass and heat transfer from rigid spheres. AIChE J. 13 (6), 1219–1221. https://doi.org/10.1002/aic.690130638.

Ishii, M., Zuber, N., 1979. Drag coefficient and relative velocity in bubbly, droplet or particulate flows. AIChE J. 25 (5), 843–855. https://doi.org/10.1002/aic.690250513.

Kamei, S., Hirata, M., 1990a. Condensing phenomena of a single vapor bubble into subcooled water. Exp. Heat Transf. 3 (2), 173–182. https://doi.org/10.1080/08916159008946385.

Kamei, S., Hirata, M., 1990b. Study on condensation of a single vapor bubble into subcooled water-Part 2; Experimental analysis. Heat Transf. - Jpn. Res. 19, 1–10.

Kim, H.J., Lee, S.C., Bankoff, S.G., 1985. Heat transfer and interfacial drag in counter current steam-water stratified flow. Int. J. Multiph. Flow 11 (5), 593–606. https://doi.org/10.1016/0301-9322(85)90081-3.

Kim, S.-J., Park, G.-C., 2011. Interfacial heat transfer of condensing bubble in subcooled boiling flow at low pressure. Int. J. Heat Mass Transf. 54 (13–14), 2962–2974. https://doi.org/10.1016/j.ijheatmasstransfer.2011.03.001.

Li, H., Tian, M., Wei, M., Zhang, J., 2022. Numerical investigation on interfacial characteristics of steam bubble condensation in subcooled water. Int. Commun. Heat Mass Transf. 132, 105886. https://www.sciencedirect.com/science/article/abs/pii/S0735193322000082.

Lilly, D.K., 1992. A proposed modification of the Germano subgrid-scale closure method. Phys Fluids A 4, 633–635. https://doi.org/10.1063/1.858280.

Lim, I.S., Tankin, R.S., Yuen, M.C., 1984. Condensation measurement of horizontal Cocurrent steam/water flow. J. Heat Transf. 106 (2), 425–432. https://doi.org/10.1115/1.3246689.

Long, S., Yang, J., Huang, X., Li, G., Shi, W., Sommerfeld, M., Yang, X., 2020. Large-eddy simulation of gas-liquid two-phase flow in a bubble column reactor using a modified sub-grid scale model with the consideration of bubble-eddy interaction. Int. J. Heat Mass Transf. 161, 120240 https://doi.org/10.1016/j.ijheatmasstransfer.2020.120240.

Lorencez, C., Nasr-Esfahany, M., Kawaji, M., 1997. Turbulence structure and prediction of interfacial heat and mass transfer in wavy-stratified flow. AIChE J. 43 (6), 1426–1435. https://doi.org/10.1002/aic.690430606.

Ma, T., Ziegenhein, T., Lucas, D., Krepper, E., Fröhlich, J., 2015. Euler-Euler large eddy simulations for dispersed turbulent bubbly flows. Int. J. Heat Fluid Flow 56, 51–59. https://doi.org/10.1016/j.ijheatfluidflow.2015.06.009.

Ma, T., Ziegenhein, T., Lucas, D., Fröhlich, J., 2016. Large eddy simulations of the gas–liquid flow in a rectangular bubble column. Nucl. Eng. Des. 299, 146–153. https://doi.org/10.1016/j.nucengdes.2015.08.010.

Marschall, H., 2011. Towards the Numerical Simulation of Multi-Scale Two-phase Flows. Ph.D. Thesis. Technische Universitat Munchen, Munich, Germany.

Nahed, J., Dgheim, J., 2019. Estimation curvature in PLIC-VOF method for interface advection. Heat Mass Transf. 56, 773–787. https://doi.org/10.1007/s00231-019-02737-4.

Pan, L., Tan, Z., Chen, D., Xue, L., 2012. Numerical investigation of vapor bubble condensation characteristics of subcooled flow boiling in vertical rectangular channel. Nucl. Eng. Des. 248, 126–136. https://doi.org/10.1016/j.nucengdes.2012.04.001.

Patel, G., Tanskanen, V., Kyrki-Rajamäki, R., 2014. Numerical modelling of low-Reynolds number direct contact condensation in a suppression pool test facility. Ann. Nucl. Energy 71, 376–387. https://doi.org/10.1016/j.anucene.2014.04.009.

Prasser, H.M., Ezsol, G., Baranyai, G., 2004a. Water Hammer Tests, Condensation Caused by Cold Water Injection into Main Steam-Line of VVER-440-type PWR – Quick-Look Report (QLR). Technical report. WAHA Loads Proj. Del., p. D48

Prasser, H.M., Ezsol, G., Baranyai, G., 2004b. Water Hammer Tests, Condensation Caused by Cold Water Injection into Main Steam-Line of VVER-440-type PWR – Data Evaluation Report (DER). Technical report. WAHA Loads Proj. Del., p. D51

Ranz, W.E., Marshall, W.R., 1952a. Evaporation from drops Part 1. Chem. Eng. Progr. 48 (3), 141–146.

Ranz, W.E., Marshall, W.R., 1952b. Evaporation from drops Part 2. Chem. Eng. Progr. 48 (4), 173–180.

Schiller, L., Naumann, A., 1933. A drag coefficient correlation. Zeit. Ver. Deutsch. Ing. 77, 318–320.

Smagorinsky, J., 1963. General circulation experiments with the primitive equations: I. The basic experiment. Mon. Weather Rev. 91 (3), 99–164. https://doi.org/10.1175/1520-0493(1963)091<0099:GCEWTP>2.3.CO;2.

Štrubelj, L., Ézsöl, G., Tiselj, I., 2010. Direct contact condensation induced transition from stratified to slug flow. Nucl. Eng. Des. 240 (2), 266–274. https://doi.org/10.1016/j.nucengdes.2008.12.004.

Strubelj, L., Tiselj, I., 2008. Numerical modelling of direct contact condensation in transition from stratified to slug flow. In: Proceedings of the Workshop on Experiments and CFD Code Application to Nuclear Reactor Safety (XCFD4NRS), Grenoble, France, pp. 10–12.

Ubbink, O., 1997. Numerical Prediction of Two Fluid Systems with Sharp Interfaces. PhD Thesis. Imperial College of Science, Technology & Medicine, London, UK.

Yadigaroglu, G., 2005. Computational fluid dynamics for nuclear applications: from CFD to multi-scale CMFD. Nucl. Eng. Des. 235 (2–4), 153–164. https://doi.org/10.1016/j.nucengdes.2004.08.044.

Yuan, D.-W., Pan, L.-M., Chen, D.-Q., Wang, X.-J., 2009. Condensation heat transfer coefficient at vapour-liquid interface of subcooled flow boiling in vertical narrow rectangular channel. Nucl. Power Eng. 30 (5), 30–34.

Zeng, Q., Cai, J., Yin, H., Yang, X., Watanabe, T., 2015. Numerical simulation of single bubble condensation in subcooled flow using OpenFOAM. Prog. Nucl. Energy 83, 336–346. https://doi.org/10.1016/j.pnucene.2015.04.011.